4. Scattering layer applied DSSC

Based on previous result, it is known the absorption of light, especially longer wavelength, is not efficient in normal DSSCs; thus different structures are proposed to enhance the absorption of light [1][2][3]. Among the suggested methods, one is the use of the "scattering layer" [3][4][5][7], which is deposited on the original nano-crystalline TiO_2 layer to elongate the effective optical path. The scattering layer is composed by TiO_2 crystal as well, but the diameter is larger, about 100nm [6]. Fig.4.1 shows the morphology of the scattering layer with its transmission data, it can be observed the transmittance in longer wavelength is lower than 24nm nano-crystalline layer. The DSSC devices incorporated the scattering layer are fabricated and corresponding photoelectrical properties are discussed in this chapter.

(a) (b)

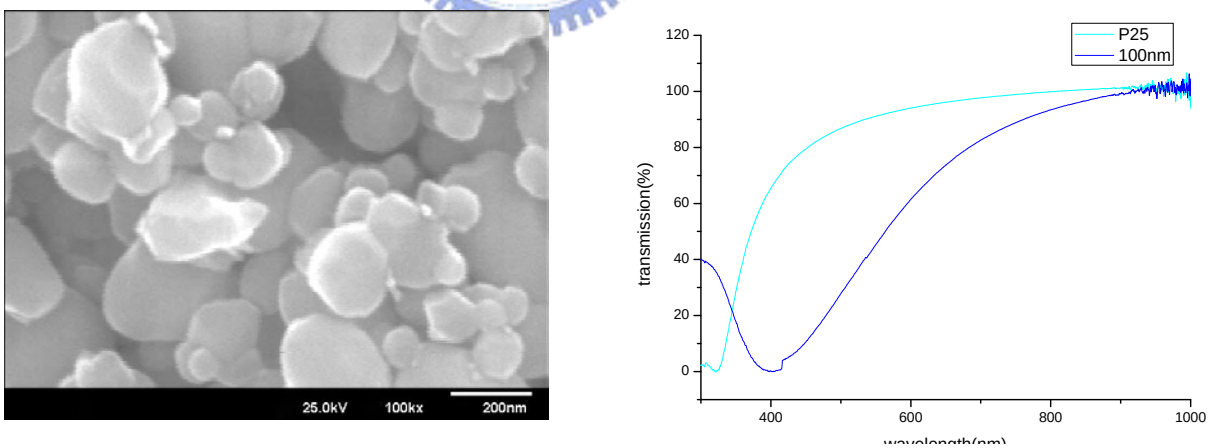

Fig.4.1 (a) the SEM image of 100nm scattering particles used in the experiment
(b) the transmission spectrum of film composed of P25 and 100nm particles

4.1 Fabrication process

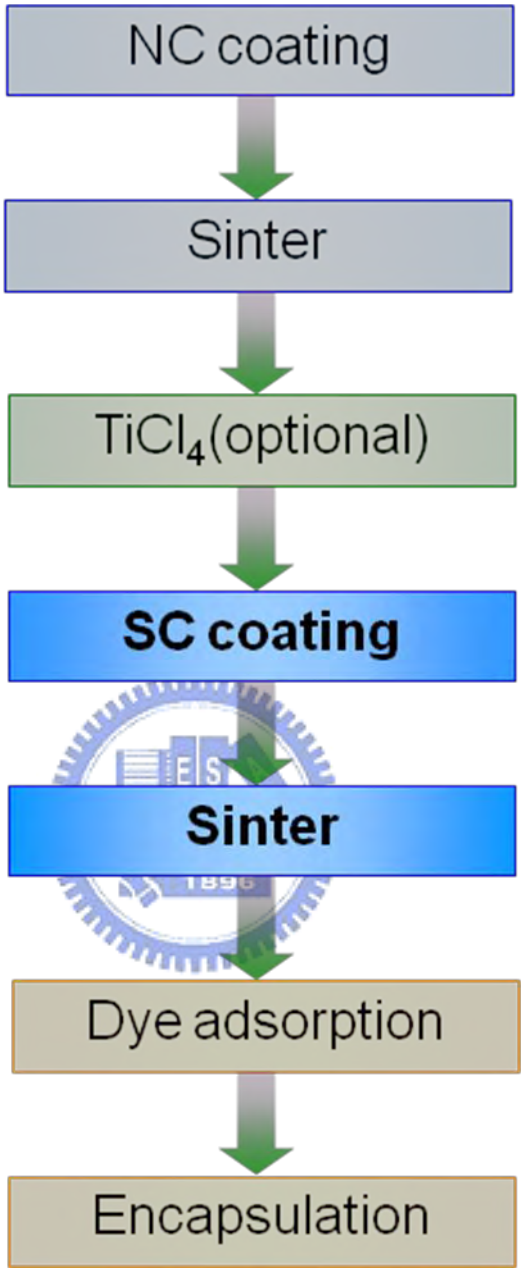

Fig.4.1.1 the fabrication flow of scattering layer applied DSSC

(a)

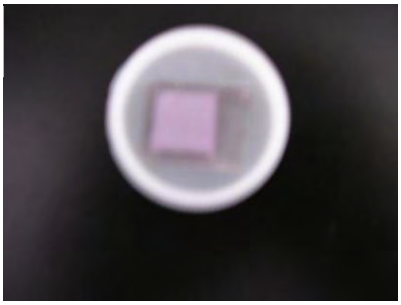

(b)

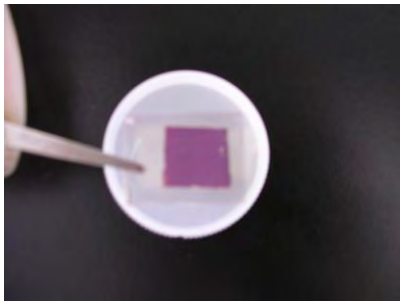

Fig.4.1.2 the pictures from (a) scattering layer side (b) bottom layer side after dyeing

The fabrication process flow is shown in Fig.4.1.1. It is almost the same as normal DSSC except for additional processes for scattering layer deposition. The paste for scattering layer deposition contains 100nm TiO_2 (98% anatase, which is not similar to P25) alpha-terpineol, and ethyl cellulose in the same weight percentage as P25 paste. Since the volume is different for crystal with different diameters, the density of the scattering layer is expected to be lower than the bottom layer such that the penetration of electrolyte should not be influenced by the additional scattering layer.

After dye adsorption, the adsorptive situation of scattering layer is obviously different from the bottom P25 layer, depicted as Fig.4.1.2 (a), (b) and this mainly relates to the internal surface area of these two different layers.

4.2 **Properties of the scattering layer**

Although the fabrication processes for scattering layer is similar to 24nm layer, very different properties are observed when the scattering layer is annealed in the same conditions as 24nm layer. Obvious aggregations of crystals are observed, as Fig.4.2.1 (a).

Because the aggregations happened during the annealing process and caused a poor uniformity film, the annealing condition is tuned to obtain an applicable scattering layer. First, the annealing temperature is lowered, and Fig.4.2.1 (b) is the film after 300℃ annealing. It is observed that the situation is different; the aggregations are reduced. Next, when the annealing temperature is modified to 270℃, a totally uniform scattering layer can be obtained, as Fig.4.2.1 (c).

When deposited on 24nm nano-crystal layer, the scattering layer aggregates less than it does on TCO layer (Fig.4.2.1 (d)). This is thought to be related to the mechanism of the aggregation, which correlates with total surface energy. The deposited bottom layer is

already in a stable morphology, and this could limit the movement of larger scattering crystals above. As an accident due to the aggregation phenomenon, the deposition situation of scattering layer on bottom layer of smaller diameter crystal can be identified from the vacancy induced near the aggregating locations (Fig.4.2.1 (e)).

A preliminary cognition of the aggregation behavior is related to the total surface energy, and it is tried to identify the variation of total energy during the sintering process. After the deposition of the scattering layer and the sintering at 270℃ for 30mins, an additional annealing step at 450℃ is applied again. It is found no obvious aggregation happens (Fig.4.2.1 (f)). Therefore, the annealing process could not only provide energy but also determine the energy variation path. This result is advantageous in the application of DSSC since the optimal sintering process has been confirmed to be done under 450℃.

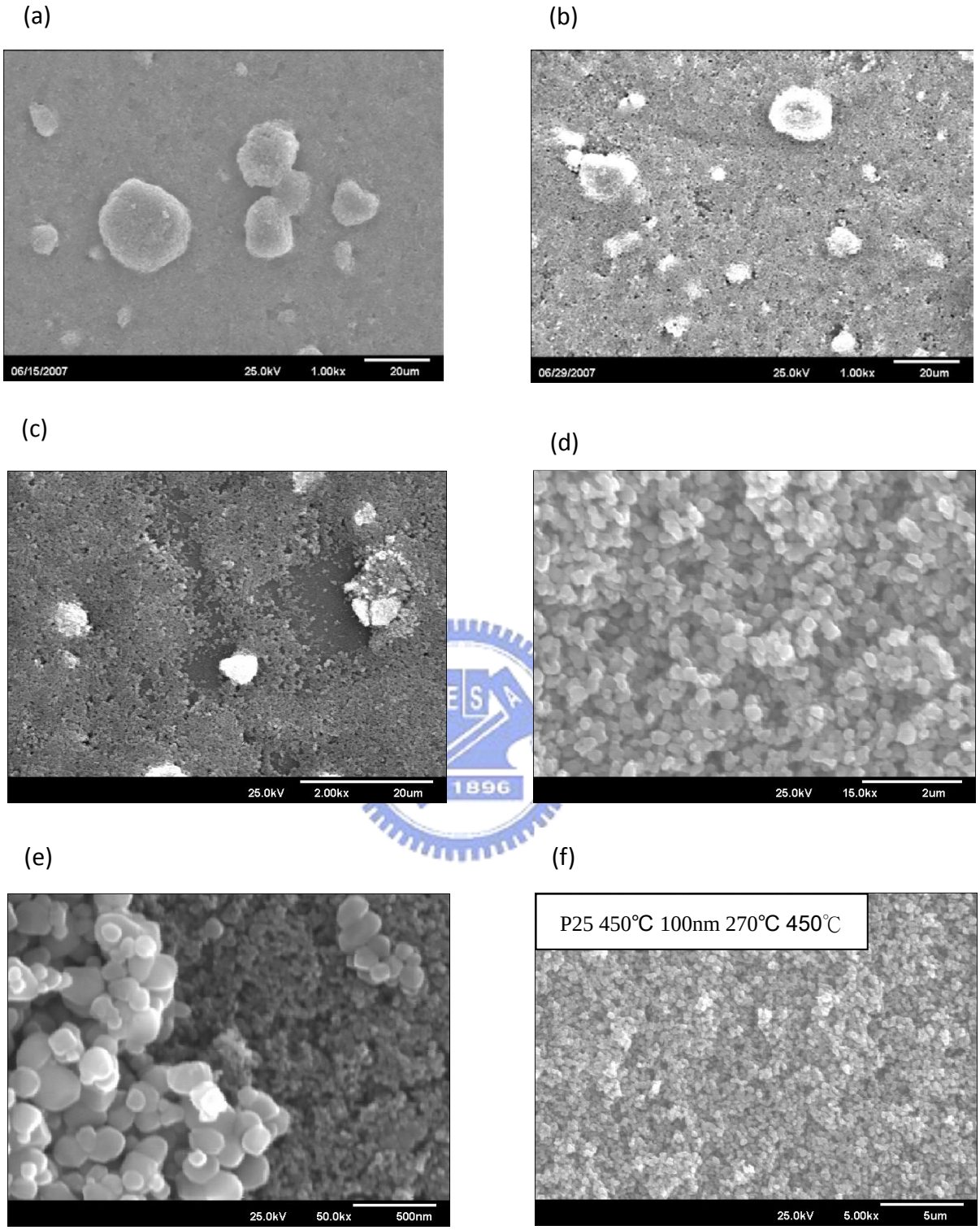

Fig.4.2.1 the morphologies of scattering layer after different heat processes

(a)450°C (b)300°C

(c)450°C on P25

(d) 270°C on P25 then 450°C

(e) comparison of the scattering layer and the bottom layer

(f)270°C

4.3 **Photo-electrical analysis**

As previously examined cases, TiO_2 bottom layer of higher transparency and normal transparency with $TiCl_4$ treatment were included in the experiment. It is suggested that the influence of scattering layer on highly transparent bottom layer be more obvious since transmitted light is in a higher ratio.

Fig.4.3.1 depicts the photocurrent and dark current for devices of high surface ratio bottom layer with and without the scattering layer. The thickness of the scattering layer is determined by the surface profiler to be 0.5um for all cases. According to the result, it is observed that the enhancements on both photovoltage and photocurrent occur when the scattering layer was applied. However, the reason of the enhancements is thought to be different from that of the treatment of $TiCl_4$ described in the last chapter. Applying the scattering layer mainly improves the photovoltage V_{oc} whereas the enhancement on photocurrent is less when compared with $TiCl_4$ cases.

Although both $TiCl_4$ treatment and the use of scattering layer induced increase both on photo voltage and photocurrent, the causes are different in the mechanisms. The purpose of the scattering layer is to delay the transmission time of incident light and thus to effectively elongate the optical path so that the absorption property of DSSC with the scattering layer can be better than the original ones. To confirm this suggestion, EIS is done for these samples, and the results are shown as Fig.4.3.2 (a). The phase-frequency plot of each case is also shown as Fig.4.3.2 (b), to distinguish the differences of the two EIS results. Differences occurred on the peak of 20 Hz and the peak of 20k Hz. According to the understanding of EIS characteristics of DSSC at present stage, the difference on 20Hz means the dye/TiO_2 interface properties are not similar for the two cases. Since the surface area of the bottom layer is much larger than the surface area of scattering layer, it is reasonable to assume the detected signal is mainly due to the dye/TiO_2 interface of the

bottom layer for both cases. For the surface areas are similar in these two conditions, and so are the amount of adsorbed dye molecules, the difference should be due to the absorptive properties, which was already examined by the EIS results of normal DSSC under varied illumination intensity in the last chapter. The light absorption of the sample with the scattering layer is therefore certain to be better than the one without the scattering layer, as it was expected. Due to the stronger absorption, more excited carriers are injected into TiO_2 and thus were accumulated to induce higher quasi Fermi level shift. Additionally, there is also a difference on 20k Hz, which represents a difference on the Pt/electrolyte interface or on the TiO_2/TiO_2 interfaces. The former one is less possible for the fabrication conditions are the same for each one, and the difference should be due to the latter one. The conjecture is about the sintering processes that influenced the grain boundaries between TiO_2 nanocrystals. Since the annealing process is applied again after the coating of scattering layer, the boundary disorders might be less and thus lead to smaller interface impedance.

Next, scattering layers on $TiCl_4$ treated devices were considered; the surface ratios of these samples were normal. Fig.4.3.3 shows the results, and it was observed the enhancement on V_{oc} is still reserved but the improvement on photocurrent is not obvious. Similarly, the EIS was examined again (Fig.4.3.4 (a)). The previously observable differences on EIS characteristics are not revealed clearly despite a difference on the series resistance, which corresponds to the slope near V_{oc}, appears. From the phase plot as Fig.4.4.4 (b), the two curves are similar as well, and only a little bit of the diversity occurred on all frequencies.

It is worth noticing that the impedances are decreased as well as the discussions in the last chapter for devices with thick bottom layer treated by $TiCl_4$, which induce more effective dye/TiO_2 charge transferring, Besides, no additional frequency shifts were observed in the phase plot, which reveals the working of the devices are stable and no

uncertainties of fabrication happened.

Additionally, the recombination and electron transport characteristics were both examined for devices with the scattering layer. Fig.4.3.5 (a) and (b) are the transient voltage results and the extracted recombination time constants at different voltage levels. The relaxation processes seem to be in similar rates, but there is a little difference, and the extracted distribution revealed the difference clearly. A transition on slope happened on the device with the scattering layer. In lower voltage region, the slope is parallel to the device without scattering layer whereas a smaller slope is in the high voltage region. Since the thicknesses of the bottom layer are close, the variation in slope could indicate that the recombination processes in the device with scattering layer be different from normal ones. It is still uncertain what the cause is, and more samples should be repeated and tested to check whether this phenomenon is popular.

The current transient characteristics are similar for these samples, as Fig.4.3.6, but the transition time of the device with scattering layer is a little slower. To identify whether if it is the result from scattering layer, another device is fabricated and measured, as the blue one inserted in the figure. It seems the transient behavior of devices with the scattering layer does not change a lot and the difference could be ascribed to the diversity of devices.

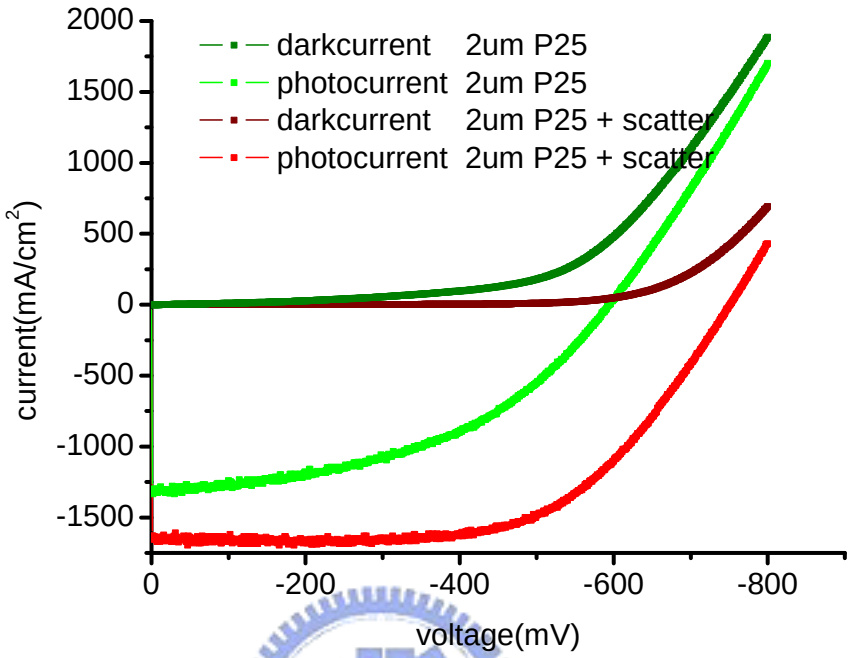

Fig.4.3.1 The photocurrent and dark current to voltage characteristics of two kinds of devices with highly transparent bottom layer: (1) P25 layer and (2) P25 layer with scattering layer, the illumination intensity is 100mW/cm^2 .

(a)

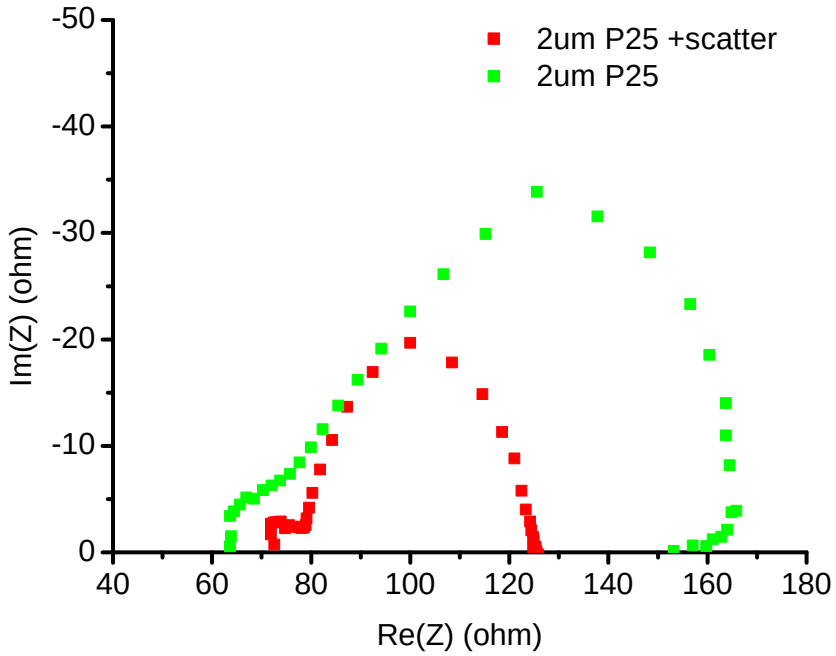

(b)

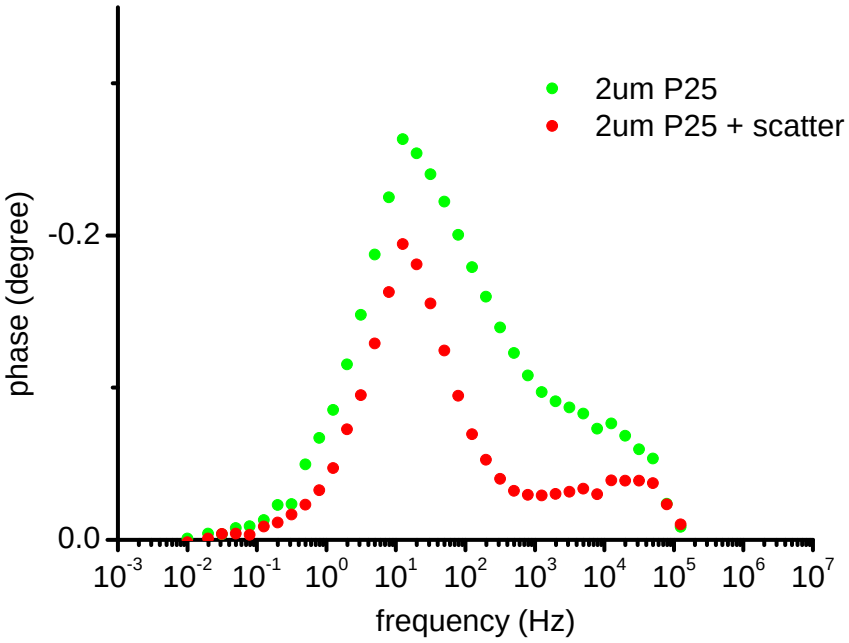

Fig.4.3.2 The (a) EIS and (b) phase plot of two kinds of devices with highly transparent bottom layer: (1) P25 layer and (2) P25 layer with scattering layer under illumination intensity 100mW/cm^2 and open circuit voltages.

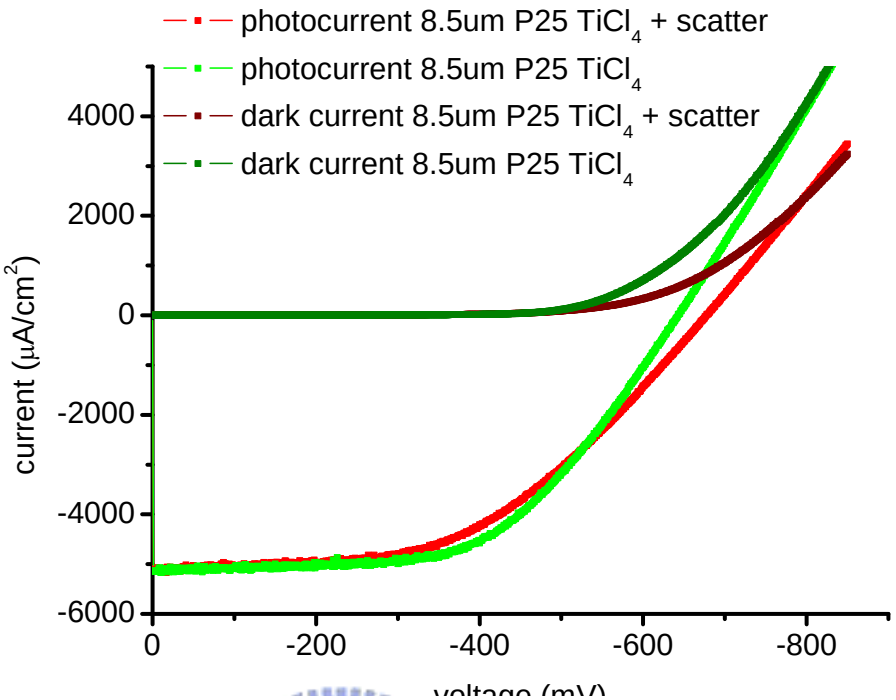

Fig.4.3.3 The photocurrent and dark current to voltage characteristics of two kinds of devices with normally transparent bottom layer: (1) P25 layer and (2) P25 layer with scattering layer, the illumination intensity is 100mW/cm^2 .

(a)

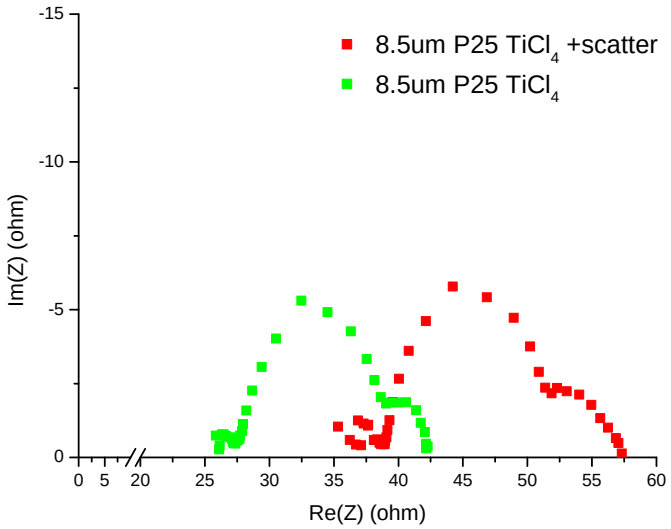

(b)

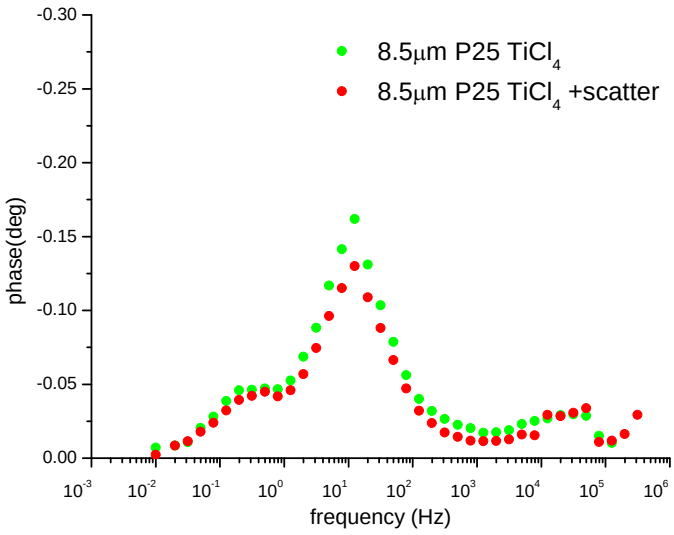

Fig.4.3.4 The (a) EIS and (b) phase plot of two kinds of devices with normally transparent bottom layer: (1) P25 layer and (2) P25 layer with scattering layer under illumination intensity 100mW/cm^2 and open circuit voltages.

(a)

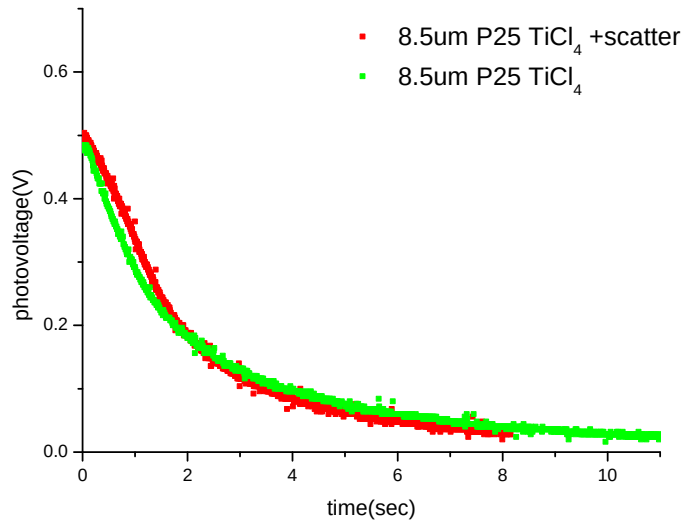

(b)

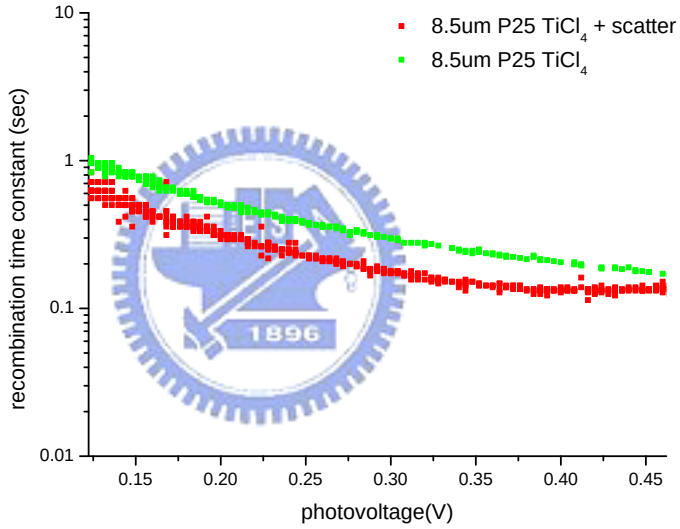

Fig.4.3.5 The (a) photovoltage transient behaviors and (b) extracted recombination time constants versus photovoltage of devices with (1) P25($TiCl_4$ treated) and (2) P25($TiCl_4$ treated) + scattering layer

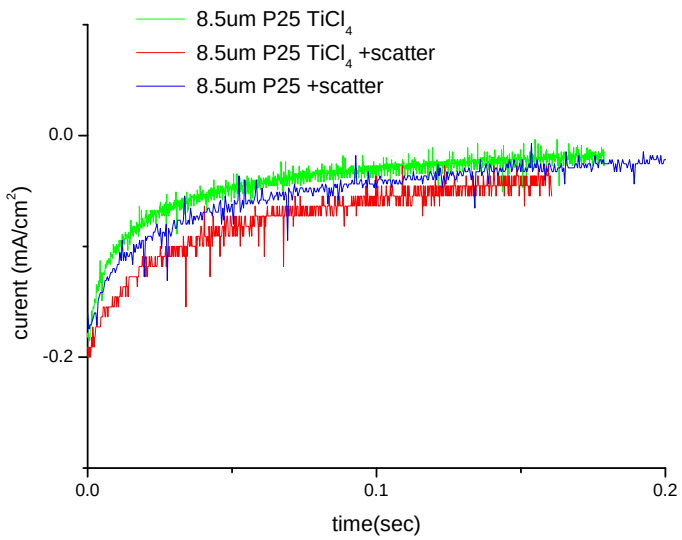

Fig.4.3.6 the photocurrent transient behaviors of three different devices

(1) P25($TiCl_4$ treated),

(2) P25($TiCl_4$ treated)+scattering layer, and

(3)P25 + scattering layer.

References

[1] A. Mihi; F. J. López-Alcaraz; H. Míguez, *App. Phys. Lett.* 2006, 88, 193110.

[2] A. Mihi and H. Mı´guez, *J. Phys. Chem. B* 2005, 109, 15968.

[3] S. Hore et al., *Solar Energy Materials & Solar Cells* 2006, 90, 1176.

[4] Z.-S. Wang et al., *Coordination Chemistry Reviews* 2004, 248, 1381.

[5] J. M. KROON ET AL., *Prog. Photovolt: Res. Appl.* 2007, 15, 1.

[6] Hironori Arakawa; Takeshi Yamaguchi; Akihito Takeuchi; Shinya Agatsuma, *Efficiency Improvement of Dye-Sensitized Solar Cell by Light Confined Effect*, 2006, IEEE.

[7] Peng Wang; Shaik M. Zakeeruddin; Pascal Comte; Raphael Charvet; Robin Humphry-Baker; Michael Gratzel, *J. Phys. Chem. B* 2003, *107*, 14336.

5. Nano-tube applied DSSC

In the 3rd and the 4th chapters, the characteristics of conventional DSSC and DSSC with application of the scattering layer were both examined. It was found that the recombination rate is efficiently inhibited by the treatment of $TiCl_4$ on TiO_2 and the absorption ability in longer wavelength of ruthenium based dye molecules was enhanced by the application of scattering layer, but for both cases, the transport characteristics are almost not changed. The transport of electrons mainly depends on concentration gradient of excess charges induced diffusion, which could be limited by the large amount of grain boundaries due to the finite size of 20nm nanocrystal. Although the recombination rate of DSSC is sub $10s^{-1}$, which is very well compared with other types of solar cells, the charge transport time is too slow, just over some milliseconds, however. This could be one of the most important factors that limited the conversion efficiency. To overcome this disadvantage, a different nanostructured TiO_2 template is applied, that is, the nanotube structure. It is thought the tube shaped structure may provide not only sufficient surface area but also continuously extended dielectric distribution in space, which is able to support electric field in the transport direction.

To apply the nanotube array to DSSC, the device structure is modified [1][2], as Fig.5.1 shows. Since the tube with sufficient length can be only fabricated on the titanium substrate now, the incident light should be in the opposite direction.

(b)

Fig.5.1 (a) the modified device structure of nanotube applied DSSC and (b) the morphology of fabricated tube array.

5.1 Fabrication process

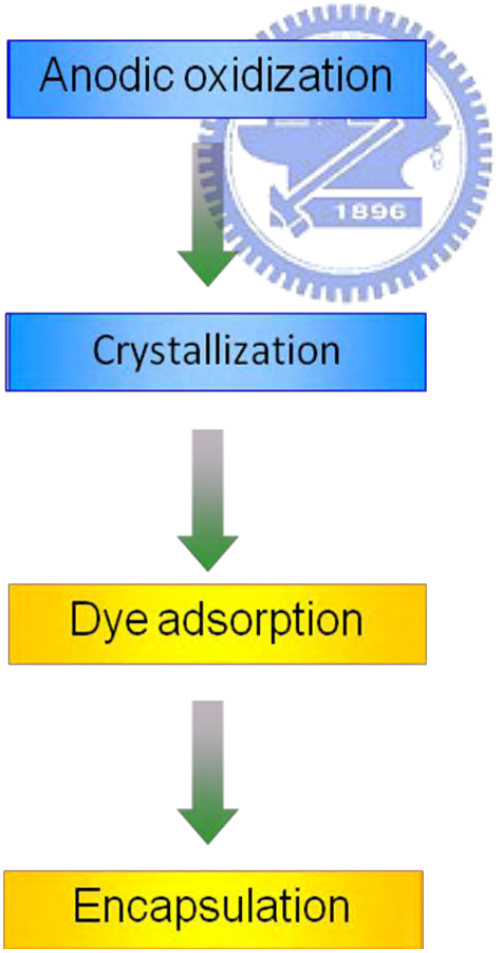

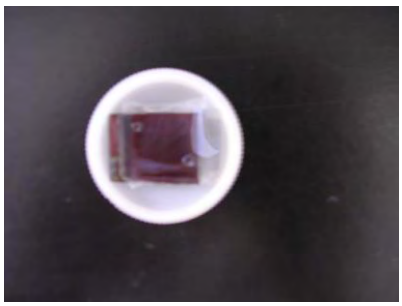

Fig.5.1.1 the fabrication flow of nanotube based DSSC (the image of the completed device is also inserted)

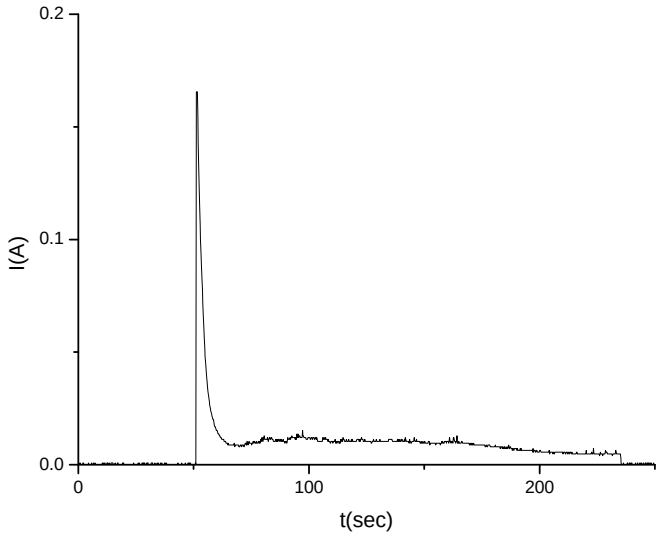

Fig.5.1.2 the oxidation current at the initial stage

The fabrication processes of nanotube applied DSSC is different from the previous ones since the device structure is modified. As the first block in Fig.5.1.1, the TiO_2 nanotube array was fabricated by anodic oxidation. The conditions of the anodic oxidation were described as follows: all of the samples were fabricated in constant voltage method; Fig.5.1.2 depicts the reaction current at the initial stages [3]. The 250um titanium foil was used as the anodic substrate and the cathode was a platinum film; the solution used in the process contained 0.25 wt% ammonium fluoride in ethylene glycol [4]. Different applied voltage and oxidation time were tested; the cause of these conditions will be discussed in next section.

Later, the fabricated tube array was heated to 450℃ in air flow for some hours. Because the initially grown TiO_2 tubes are amorphous, the annealing is necessary for crystallization and the period is longer than the sintering of nanocrystalline film; the crystallization time is set to be 5 hours in the experiment afterward. After that, the dye is adsorbed onto the tube surface by similar methods before.

The counter electrode is different from previous one; the thickness of the deposited Pt film was decreased since the substrate of Ti foil is not transparent, and the light should be incident from the counter side. The deposited Pt film was as thin as 2nm such that the counter electrode can be a semi-transparent one. Finally, the encapsulation processes were all as normal ones and are not mentioned again. The outlook of the completed device is inserted in Fig.5.1.1.

5.2 Properties of TiO_2 nano-tube

The principle of the formation of TiO_2 nanotube array by anodic oxidation is fundamentally the same as the formation of nano sized pore on Ti or Al, which have been well developed. The basic chemical processes can be summarized as follows [5]:

(1) Oxide growth at the surface of the metal occurs due to interaction of the metal with O_2^- or OH^- ions [6]. After the formation of an initial oxide layer, these anions migrate through the oxide layer to reach the metal/oxide interface where they react with the metal.

(2) Metal ion (Ti^{4+}) migrates from the metal at the metal/oxide interface; Ti^{4+} cations will be ejected from the metal/oxide interface under the application of an electric field that move towards the oxide/electrolyte interface.

(3) Field assisted dissolution of the oxide at the oxide/electrolyte interface [6][7]. Due to the applied electric field the Ti–O bond undergoes polarization and is weakened promoting dissolution of the metal cations. Ti^{4+} cations dissolve into the electrolyte, and the free O_2^- anions migrate towards the metal/oxide interface, see process (1), to interact with the metal [8][9].

(4) Chemical dissolution of the metal, or oxide, by the acidic electrolyte also takes place during anodization. Chemical dissolution of titania in the HF electrolyte plays a

key role in the formation of nanotubes rather than a nanoporous structure.

The overall chemical reactions during the formation of TiO_2 layer ((1)-(2)) are:

$$2H_2O \rightarrow O_2 + 4e^- + 4H^+$$

$$Ti + O_2 \rightarrow TiO_2$$

whereas the dissolution of TiO_2 in the electrolyte is:

$$TiO_2 + 6F^- + 4H^+ \rightarrow TiF_6^{2-} + 2H_2O$$

The formation of the tube shaped structure during the oxidation and dissolution can be separated to five stages [10]. As depicted in Fig.5.2.1, after a thin oxide layer formed on the surface of Ti foil (a), small pores begin to occur on the oxide surface due to local dissolution (b) (Fig.5.2.2), the oxide on the locations of the pores will be thinner and this will cause the distribution of field be stronger there. Later, the field assisted dissolution will cause the pore become deeper as (c); the processes of (b) and (c) are repeated, and thus the straight channels are formed. It is thought there are metallic regions between the pores and these regions will be etched to produce voids when the pores become deeper (d). Afterward, the voids and the pores grow in equilibrium and the tubes are formed therefore (e). The nanotube length increases until the electrochemical etch rate equals the chemical dissolution rate of the top surface of the nanotubes. In the moment, the nanotube length will be independent of the anodization duration, as determined for a given electrolyte concentration and anodization potential [11].

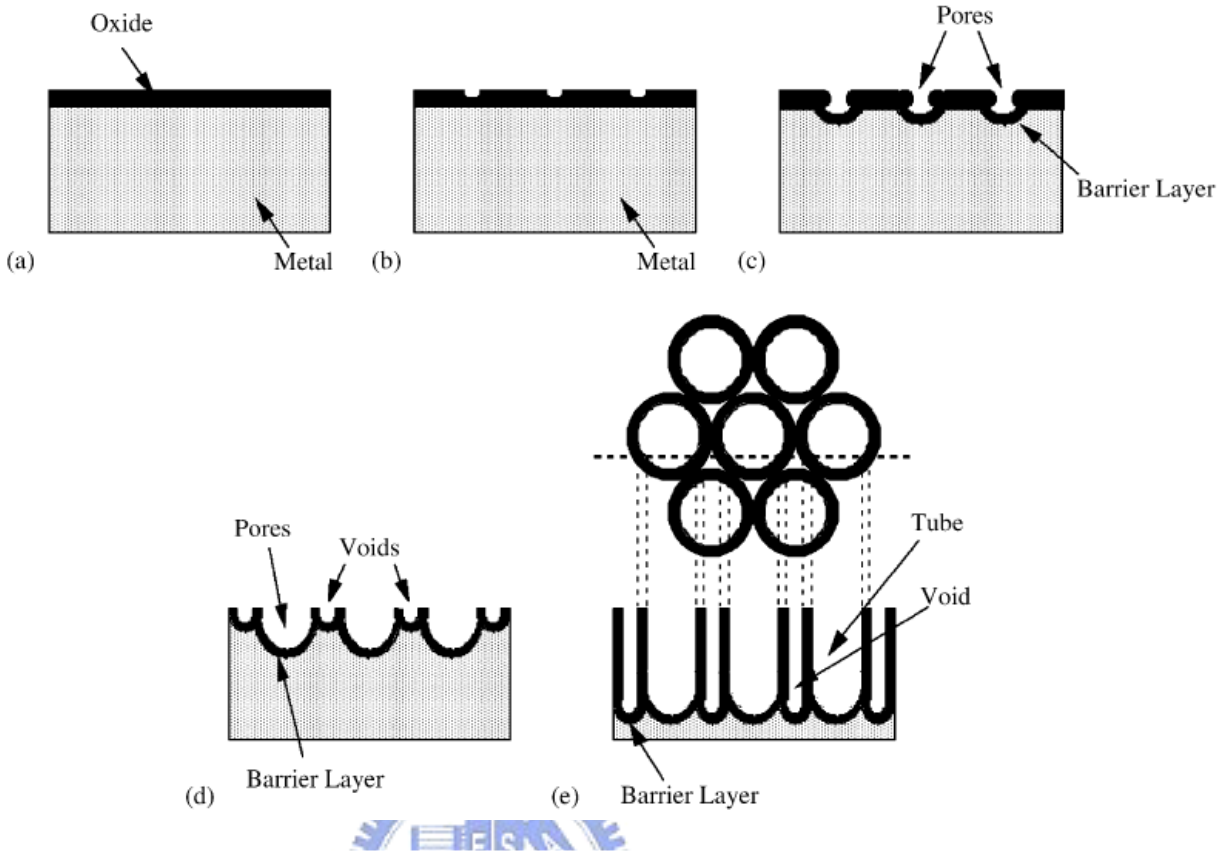

Fig.5.2.1 the different stages of the formation of the tube structure at constant voltage (a) metal surface oxidized, (b) small pores formed on the oxide, (c) the small pores are deepen by the enhanced etch rate, (d) voids in the region between pores are formed, (e) both the pores and voids are stably deepen, and thus tube structure can be produced.[5]

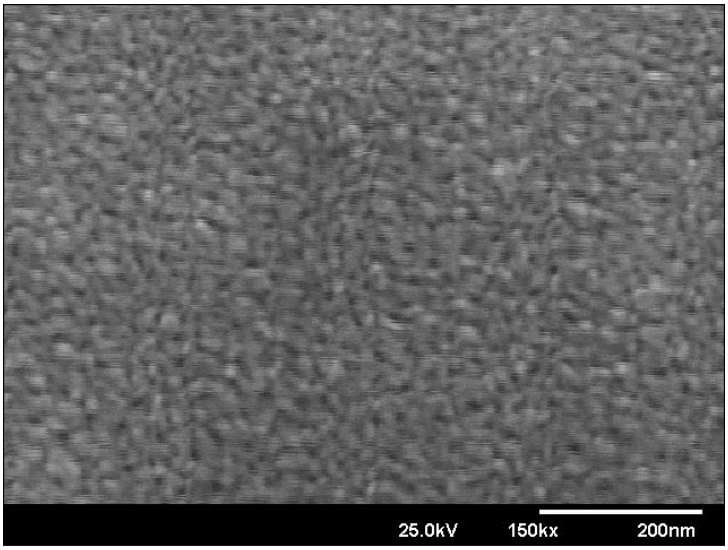

Fig.5.2.2 the small pores formed on the oxide initially

Fig.5.2.3 (a)-(e)[10] show the morphologies of the nanotube anodized by different biased potential. The dependence of the diameter on applied potential can be observed, which can be explained by the mechanisms of the tube growth described before. Since the formation of the tube is in equilibrium of dissolution and reaction, the reaction rate under higher bias should be faster while the dissolution rate remains the same for the concentration of electrolyte is maintained. Therefore, to reach the equilibrium, the ratio of reacted agents will increase as the increase potential and induce the increase in diameter. Fig.5.2.4 is a statistics about the dependence of diameters on applied potentials.

It is thought the fabrication periods in the experiments are all shorter than the time required to reach the final length since previously reported length in the same electrolyte with the same concentration is over 100 um, and it is necessary to justify the tube length after oxidization. Fig.5.2.5 shows different lengths fabricated under 40V with varied periods, it should be noticed there is some deformation at the end of the longer tubes.

The TiO_2 tubes just after fabricated are all amorphous ones, and as the XRD results in Fig.5.2.6 (a), only Ti signals are observed. Therefore, post annealing for crystallization is necessary. Fig.5.2.6 (b) and (c) are the XRD results for tubes after 400℃ 5hrs and 450 ℃ 5hrs. crystalline signals at 25.2° could be apparently observed [12], which is the anatase phase of TiO_2. Dissimilar to TiO_2 bulk or nanocrystal situations as Fig.5.2.6 (d), TiO_2 in rutile crystalline phase are not observed even after 450℃ annealing. This could be an advantageous one since the anatase is more preferred in the applications of DSSC.

(a)

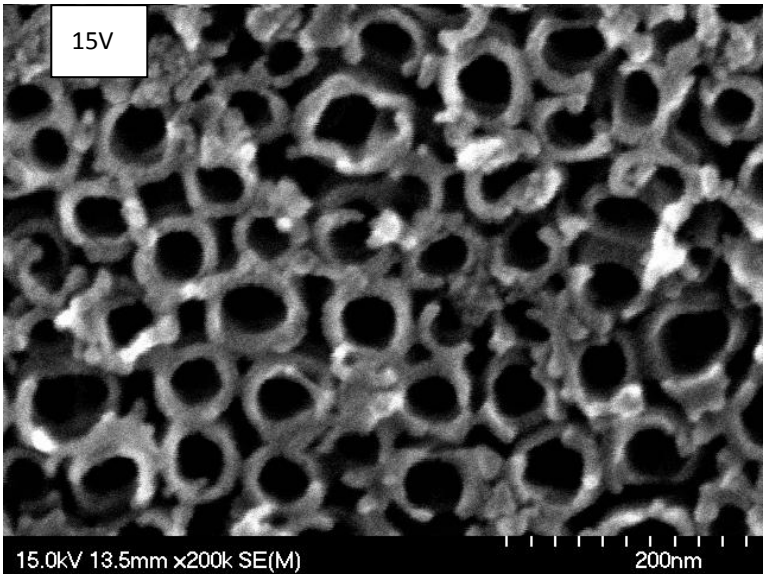
15V
15.0kV 13.5mm x200k SE(M)
200nm

(b)

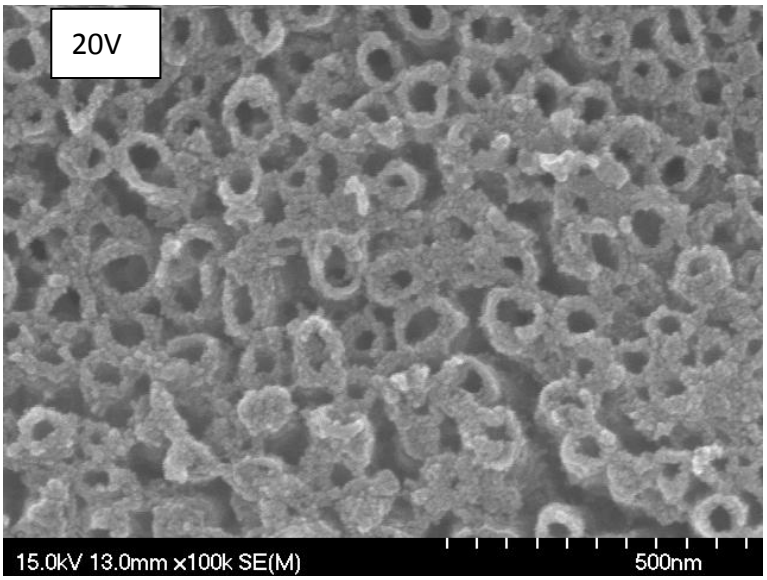
20V
15.0kV 13.0mm x100k SE(M)
500nm

(c)

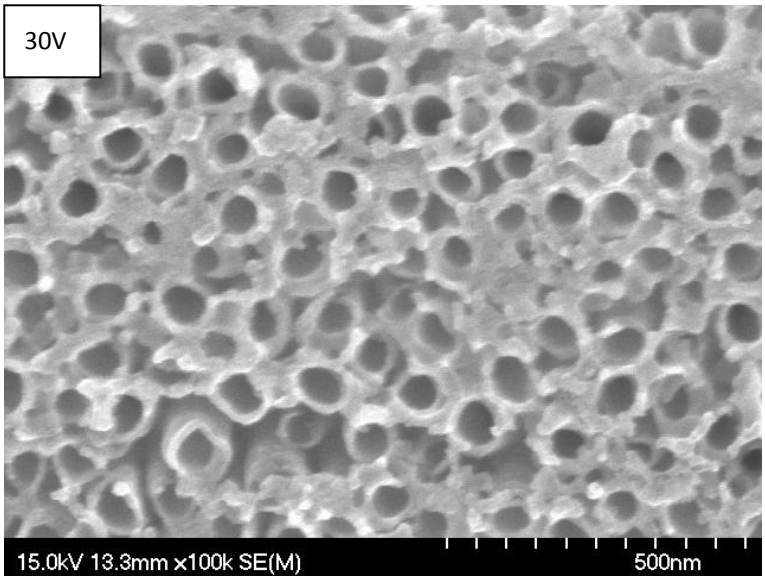
30V
15.0kV 13.3mm x100k SE(M)
500nm

(d)

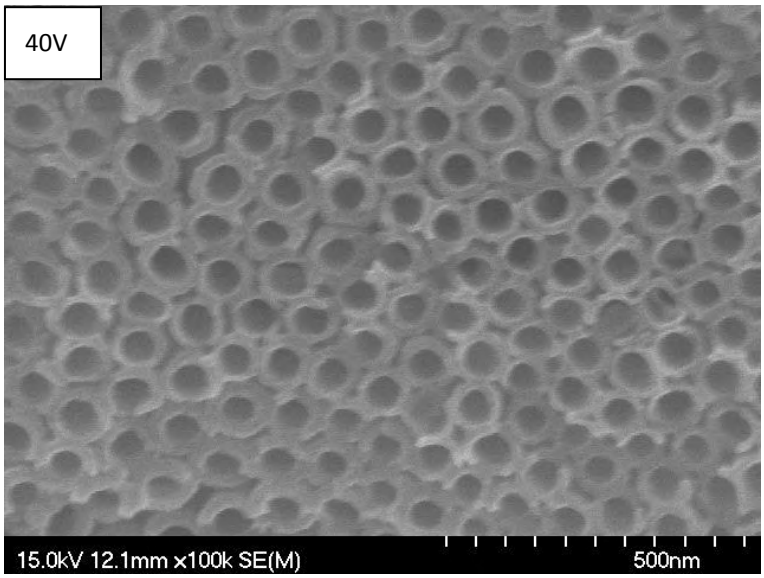

(e)

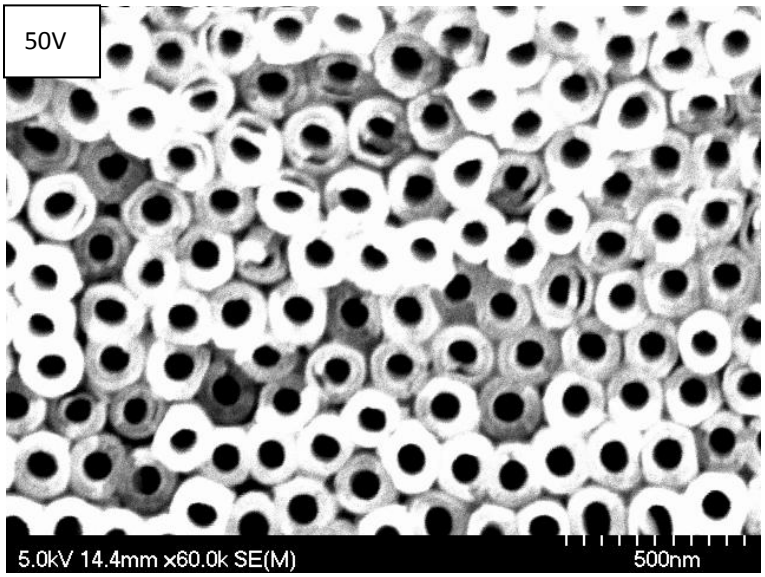

Fig.5.2.3 images of TiO_2 tube anodized under different potentials (a)15V (b)20V (c)30V (d)40V (e)50V

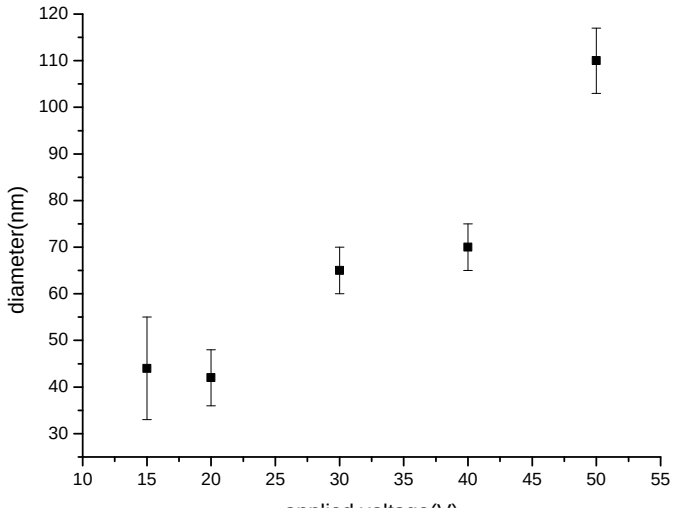

Fig.5.2.4 the dependence between tube diameter and oxidization potential

(a)

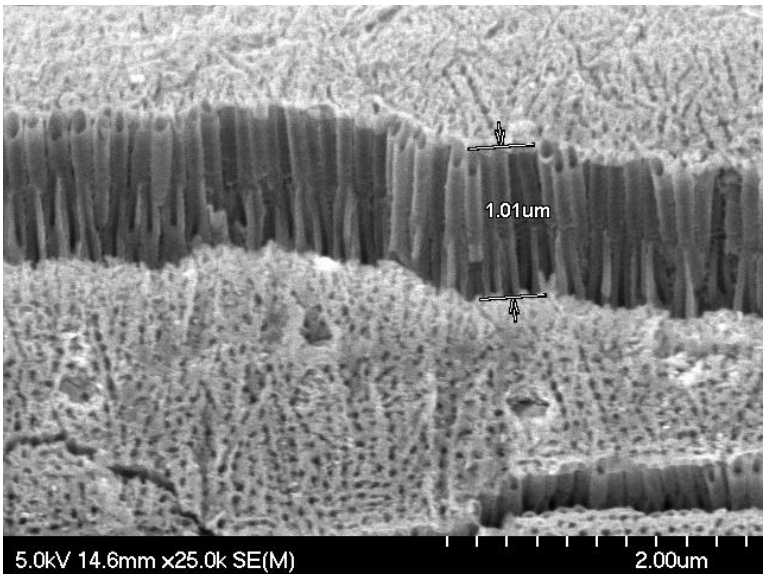

(b)

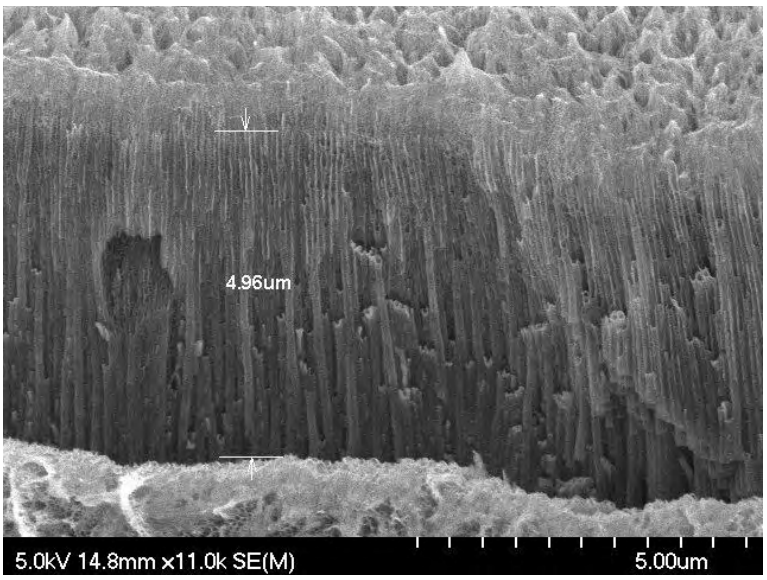

Fig.5.2.5 The tube lengths described in the article are all determined by SEM images, tubes fabricated at 40V with different periods result in (a) 1μm and (b)5μm.

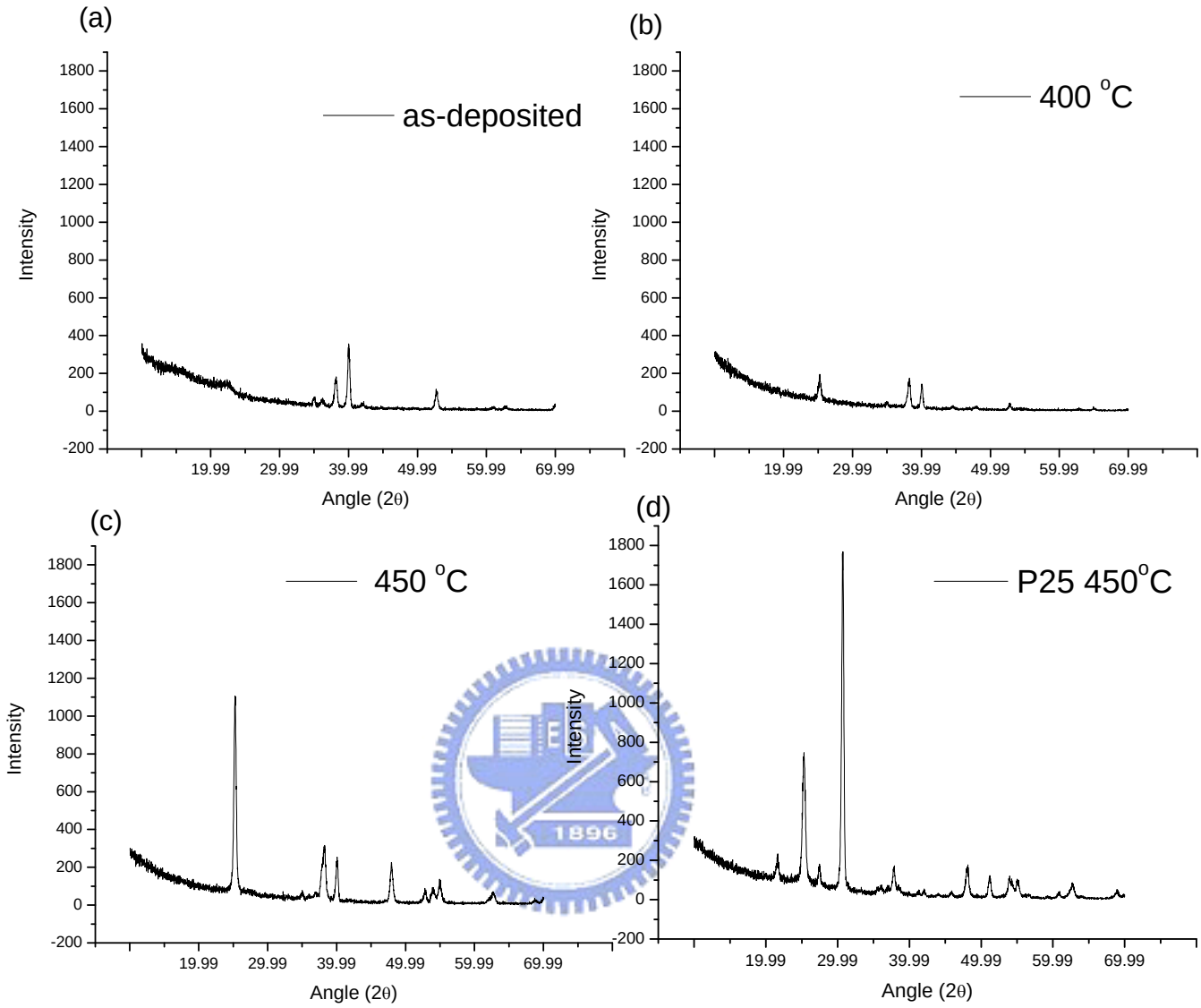

Fig.5.2.6 The crystalline characteristics are changed with applied crystallization conditions (a) as deposited, amorphous, (b) 400°C 5hrs, anatase signal occurs, (c)450°C 5hrs, anatase signal stronger, (d) the crystalline properties are different from the nanocrystal case, where both anatase and rutile signals were observed.

5.3 **Photo-electrical analysis**

At first, the tube array is fabricated with 40V applied voltage for device use. Samples with different lengths 1um and 5um are fabricated; Fig.5.3.1 shows corresponding dark current and photocurrent. The photovoltage are similar for the devices whereas the difference on photocurrent is obvious. The photovoltage remain since both samples are anodized in the same potential, and the average tube diameters are distributed in similar range. Thus, the surface to volume ratio should be also close to each other. While the adsorbed dye is proportional to the surface area, the injected excited electrons should also be proportional to the surface area if the incident intensity is sufficient that is approximately right since the illumination intensity is standard 100mW/cm^2 and the absorption layer is not thick. Then, the excess charge density, which is the amount of excess charge in unit volume, is proportional to the surface to volume ratio, so the electron quasi Fermi level shift is expected to be close and result in the observed similarity in photovoltage.

According to previous results, it is estimated that the increase in photocurrent should be due to the increase of total surface area and thus lead to increased total excess electrons from the increased amount of adsorbed dye. To confirm the estimation, EIS is done as Fig.5.3.2(a); a difference in the amount of impedance is obvious in the Nyquist plot, but it should be noticed that for both conditions, the phase plot Fig.5.3.2(b) reveals a wide peak at 2Hz, where is not a characteristic frequency in nanocrystal cases, and a little shift can be justified among the two curve in the figure. The reason for this phenomenon is revealed when the phase plot is compared with the nanocrystal ones, as Fig.5.3.2(c). The widen peak should be the superposition of the peak at 20Hz and 0.3Hz, and the difference on that peak means there are differences on both 20Hz and 0.3Hz peaks, which is the result from increasing of surface area.

Once the light harvesting behaviors for DSSC with nanotubes are observed, the recombination and transport properties are tried to be characterized. Thus, transient photovoltage and photocurrent measurement are done. Fig.5.3.3shows the recombination time constants distribution of 40V anodized 5um tubes; also inserted are the recombination time constants of P25 and P25 treated by $TiCl_4$, which are discussed before. An apparently large recombination time is seen in the figure for nanotube array as previously reported result [12]. It is an unexpected result. At present stage, the reason for this is thought to be related to the different crystallization properties observed previously and the truth that causes this property is worth being researched since the much longer recombination time is beneficial in the operation of DSSC. On the other hand, the photocurrent transient is shown in Fig.5.3.4, of which the behavior is not as expected; the transient time is longer than the nanocrystal situations and a difference near two orders exists. The origin of this phenomenon is still not clear, but it will be discovered in the future works.

Next, because it is known the surface area is not sufficient for tubes by 40V, tubes in 20V are used to fabricate DSSC. When the wall thicknesses are assumed to be the same, about 50% increase in surface area can be obtained. Fig.5.3.5 shows the change in I-V characteristics for different tube diameters. Unlike the situation in Fig.5.3.1, there are enhancements on both photovoltage and photocurrent, not only photocurrent. As previously analyzed, tube with smaller diameter provides higher surface on the same area, and on the other hand, the surface to volume ratio is also higher for lower diameters, about 30%, which induce the enhancement on the photovoltage.

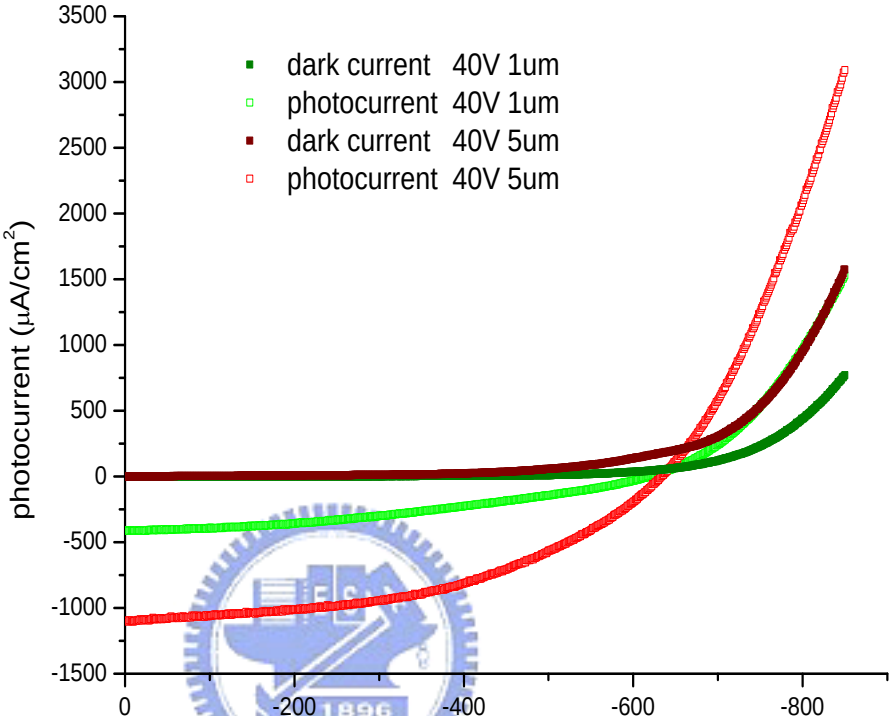

Fig.5.3.1 The photocurrent and dark current to voltage characteristics of two kinds of devices composed of nanotube with the same diameters but different tube lengths (1) 1um at 40V applied potential and (2) 5um at 40V applied potential, the illumination intensity is 100mW/cm^2 .

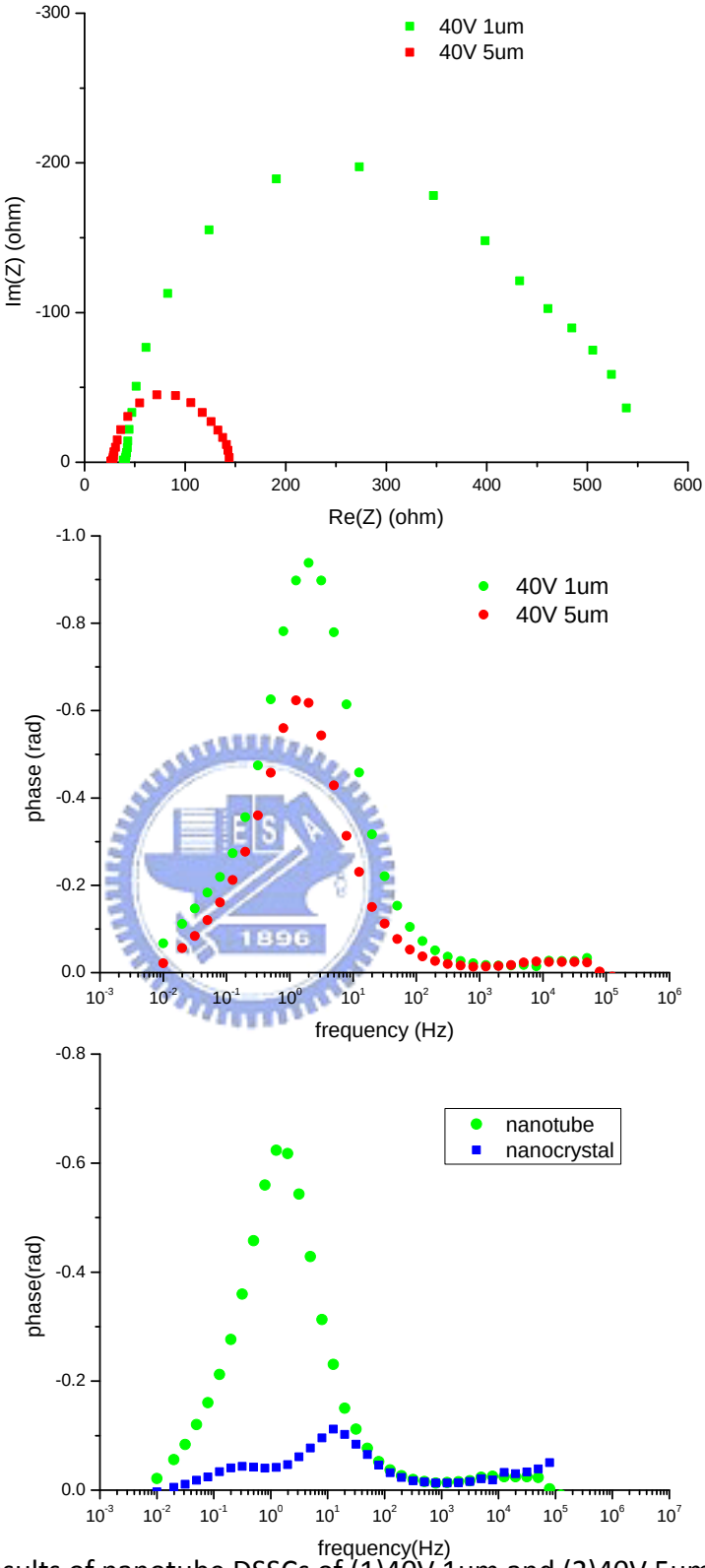

Fig.5.3.2 the EIS results of nanotube DSSCs of (1)40V 1um and (2)40V 5um (a) the Nyquist plot, the impedance value are changed and (b) the primary difference is on certain frequency and (c) the variation on the frequency is thought to be a simultaneous change on two interfaces compared with nanocrystalline cases.

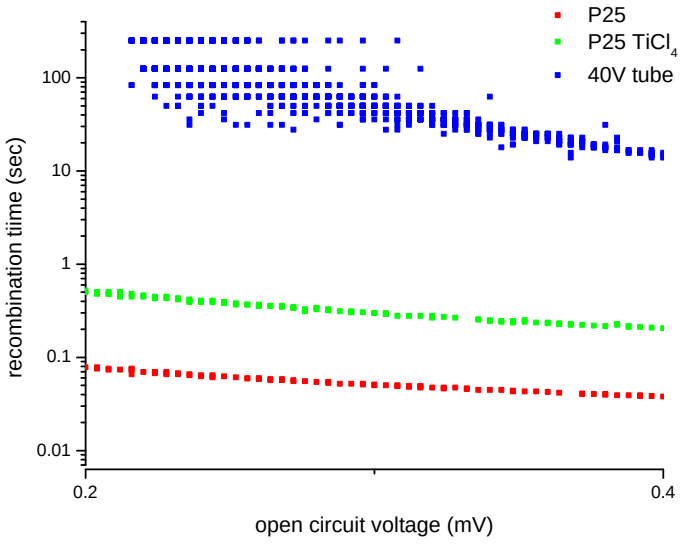

Fig.5.3.3 the recombination time constants of nanotube case are very different to nanocrystalline ones. The difference is near two orders.

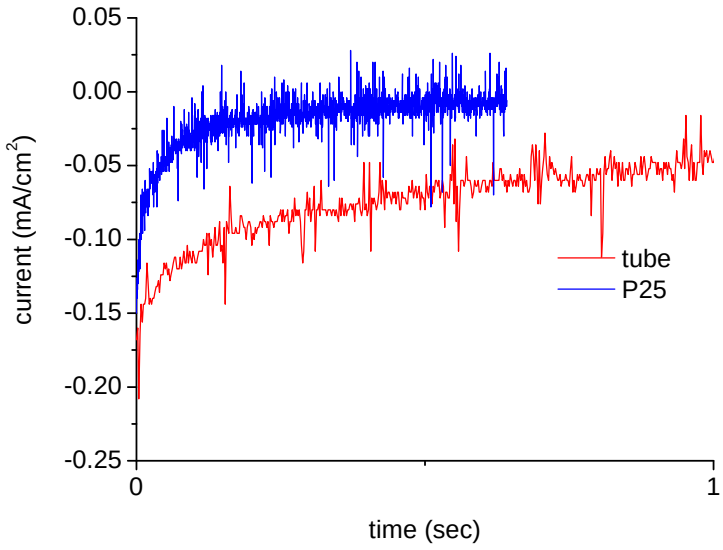

Fig.5.3.4 photocurrent transient behaviors of nanotube DSSC is slower, when compared to nanocrystalline cases; it is an unwanted results, and discovery of the reason and improvement is necessary.

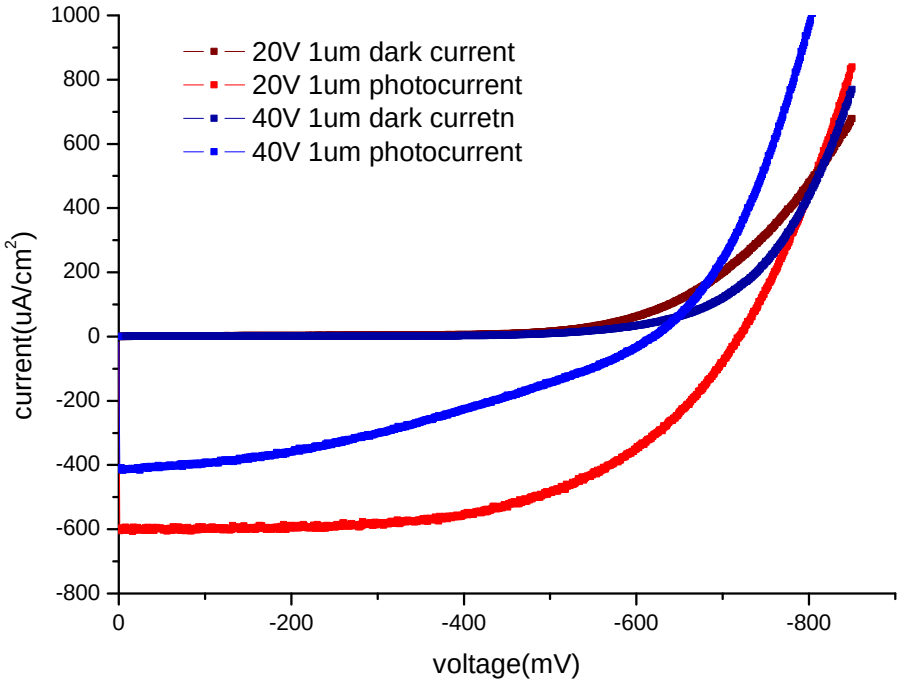

Fig.5.3.5 The photocurrent and dark current to voltage characteristics of two kinds of devices composed of nanotube with different diameters but the same tube lengths (1) 1um at 20V applied potential and (2) 1um at 40V applied potential, the illumination intensity is 100mW/cm^2.

References

[1] Gopal K. Mor; Karthik Shankar; Maggie Paulose; Oomman K. Varghese; Craig A. Grimes; *Nano Lett*. 2006, Vol. 6, No. 2.

[2] Maggie Paulose; Karthik Shankar; Oomman K Varghese; Gopal K Mor; Brian Hardin; Craig A Grimes, *Nanotechnology* 2006, 17, 1446.

[3] Gopal K. Mor; Oomman K. Varghese; Maggie Paulose; Craig A. Grimes, *Adv. Funct. Mater.* 2005, 15, 1291.

[4] Maggie Paulose; Karthik Shankar; Sorachon Yoriya; Haripriya E. Prakasam; Oomman K. Varghese; Gopal K. Mor; Thomas A. Latempa; Adriana Fitzgerald; Craig A. Grimes, J. *Phys. Chem. B 2006*, Vol. 110, No. 33.

[5] G.K. Mor et al., *Solar Energy Materials & Solar Cells* 2006, 90, 2011.

[6] V.P. Parkhutik; V.I. Shershulsky, *J. Phys. D: Appl. Phys*. 1992, 25, 1258.

[7] D.D. Macdonald, *J. Electrochem. Soc.* 1993, 140, L27.

[8] J. Siejka; C. Ortega, *J. Electrochem. Soc.: Solid State Sci. Technol.* 1977, 124, 883.

[9] G.E. Thompson, *Thin Solid Films* 1997, 297, 192.

[10] Young-Taeg Sul; C.B. Johansson; Y. Jeong; T. Albrektsson, *Med. Eng. Phys.* 2001, 23, 329.

[11] S. Chen; M. Paulose; C. Ruan; G.K. Mor; O.K. Varghese; D. Kouzoudis; C.A. Grimes, *J. Photochem.Photobiol.* 2006, 177, 177.

[12] Kai Zhu; Nathan R. Neale; Alexander Miedaner; Arthur J. Frank, *Nano Lett.* 2007, Vol. 7, No. 1.

6. Summary and Outlooks

Dye sensitized solar cell, as a photoelectrochemical device, has remarkable light harvesting properties when fabricated from inexpensive methods and materials, which are the critical elements for an applicable solar cell. In this article, the basic DSSC, scattering layer applied DSSC and nanotube applied DSSC are fabricated, and photoelectrical properties are characterized for each one.

As the beginning of the experiment, various factors in the fabrication of DSSC are examined, including the substrate resistance, the electrolyte viscosity, and the solvent used in the formation of TiO_2 paste. Later, the treatment of $TiCl_4$ is implicated; improvements on photoelectrical characteristics are measured, and the variation caused by the treatment is deduced by photoelectrical methods to be the inhibition of surface density of states which increase the recombination time about an order.

Next, to enhance the absorption property of the dye on the nanoporosu film, scattering layer is implicated and applied to DSSC use. The experimental condition to derive a uniformly distributed scattering layer is assured, and the improvement on device behaviors is also observed after the appliance of the scattering layer. Although both of $TiCl_4$ treatment and scattering layer induce enhancements, the reasons are fundamentally different, and these are identified well from the combination of different photoelectrical methods.

Afterward, it is recognized a different structure might be used to raise the charge collection efficiency. Therefore, TiO_2 nanotube array is fabricated from anodic oxidation and applied to DSSC. The relationship between morphologies of tube and applied potential are examined. From corresponding photoelectrical behaviors, the increase on effective surface area and increase on the area to volume ratio are certain for tube fabricated in lower voltage. The unexpected observations on the recombination time constants and on the diffusion time

constants are necessary to be clarified.

Additionally, DFT calculations are done for the ruthenium based dye and the adsorption of TiO_2 surface, which is prepared for the work that will be executed in the future. At present stage, the conversion efficiencies are not good enough for both nanocrystal and nanotube ones. Inducted from previous results, the reason for the lower performance of nanocrystal DSSC should be due to the decreased porosity, and this will be tried to be overcome later.

The disadvantage of DSSC now is mainly on the long time stability. Sunlight caused material degradations are thought not happened in DSSC, but the degradation on the sealant is hard to avoid and will cause the leakage of electrolyte, which is the major problem. To overcome the drawback, it seems necessary to apply solid materials to substitute the originally used electrolyte. Efforts until now have shown new problems occur in solid state DSSCs, which lead to lower performances. The applications of the developed structures are under evaluation. It is believed the performance and the stability of DSSC can be enhanced more and a photovoltaic device that can be used more conveniently is obtainable.

簡　　歷

姓 名　　：　郭宇彥

性 別　　：　男

生 日　　：　民國七十三年八月六日

出 生 地　：　臺灣新竹市

學 歷　　：　國立交通大學　電子工程學系

（ 91 年 9 月　~　95 年 6 月 ）

國立交通大學　電子研究所

（ 95 年 9 月　~　97 年 6 月 ）

碩 士 論 文:

對染料敏化太陽能電池之結構調整與相應電子行為分析

Study of Electron Behaviors in Structure Modified Dye Sensitized Solar Cells